

# Performance of the micro-PIC gaseous area detector in small-angle X-ray scattering experiments

Kaori Hattori,<sup>a,b\*</sup> Ken'ichi Tsuchiya,<sup>a,b</sup> Kazuki Ito,<sup>b</sup> Yoko Okada,<sup>a</sup> Kotaro Fujii,<sup>c</sup> Hidetoshi Kubo,<sup>a,b</sup> Kentaro Miuchi,<sup>a,b</sup> Masaki Takata,<sup>b,d,e</sup> Toru Tanimori<sup>a,b</sup> and Hidehiro Uekusa<sup>c</sup>

<sup>a</sup>Department of Physics, Kyoto University, Kyoto 606-8502, Japan, <sup>b</sup>Structural Materials Science Laboratory, RIKEN Harima Institute/SPring-8 Center, 1-1-1 Kouto, Sayo-gun, Hyogo 679-5148, Japan, <sup>c</sup>Department of Chemistry and Materials Science, Tokyo Institute of Technology, 2-12-1 Ookayama, Meguro, Tokyo 152-8551, Japan, <sup>d</sup>SPring-8/JASRI, 1-1-1 Kouto, Sayo-cho, Sayo-gun, Hyogo 679-5148, Japan, and <sup>e</sup>Department of Advanced Materials Sciences, Graduate School of Frontier Sciences, The University of Tokyo, 5-1-5 Kashiwanoha, Chiba 277-8561, Japan.  
E-mail: hattori@cr.scphys.kyoto-u.ac.jp

The application of a two-dimensional photon-counting detector based on a micro-pixel gas chamber ( $\mu$ -PIC) to high-resolution small-angle X-ray scattering (SAXS), and its performance, are reported. The  $\mu$ -PIC is a micro-pattern gaseous detector fabricated by printed circuit board technology. This article describes the performance of the  $\mu$ -PIC in SAXS experiments at SPring-8. A dynamic range of  $>10^5$  was obtained for X-ray scattering from a polystyrene sphere solution. A maximum counting rate of up to 5 MHz was observed with good linearity and without saturation. For a diffraction pattern of collagen, weak peaks were observed in the high-angle region in one accumulation of photons.

**Keywords:** gaseous detector; micro-pattern detector; small-angle X-ray scattering; SPring-8.

## 1. Introduction

Small-angle X-ray scattering (SAXS) is useful for investigating structural scales of size 1–100 nm. It is especially well suited for determining the shape and size distribution of particles, as well as the electron density fluctuation of a system. Its application in fields such as biology, material science and the study of soft condensed matters is becoming increasingly popular. Based on the analysis of SAXS patterns, the requirements for an X-ray detector are a high sensitivity, a good spatial resolution, a wide dynamic range, a large active area and operational stability for a long duration. Typically, there are two kinds of X-ray detectors: counting-type and integration-type. In the early 1980s, position-sensitive gas proportional counters (PSPC) were used for SAXS experiments in most synchrotron radiation facilities and laboratories. The PSPC is a one-dimensional photon-counting-type gaseous detector. It can attain a counting rate of only  $10^4$ – $10^5$  counts  $s^{-1}$  and has a poor spatial resolution, limited by the speed of its electronics. Third-generation synchrotron radiation sources have been available since the mid-1990s, making high-intensity and high-brilliance X-ray beams accessible. Most counting-type detectors have no tolerance for operating under such conditions. To satisfy such requirements at third-generation synchrotron radiation sources, charge-coupled device (CCD)-based X-ray detectors (Gruner *et al.*, 2002) have found wide use as integration-type X-ray detectors for

SAXS experiments and macromolecular crystallography. They are free from counting limitations caused by electronics and are thus suitable for intense X-ray radiation. However, integration-type X-ray detectors have an intrinsic limitation in the signal-to-noise ratio of their data caused by internal noise such as readout noise and dark current in the CCD, except for quantum fluctuation of the signal. To solve this problem, photon-counting-type gaseous detectors have been developed using micro-pattern technologies. They have dramatically improved the signal-to-noise ratio. Since the late 1990s a micro-strip gas chamber (MSGC) (Oed, 1988; Tanimori *et al.*, 1996), a photon-counting-type gaseous detector, has been developed and studied at SPring-8, the world's largest third-generation synchrotron radiation source.

Gaseous detectors have also been employed as two-dimensional X-ray position-encoding instruments (Smith, 2006, and references therein). A classical example can be observed in X-ray protein crystallography, wherein two-dimensional multi-wire proportional counters (MWPC) were being used in many synchrotron radiation facilities in the 1980s (Phizackerley *et al.*, 1986). However, limitations in counting rates and position resolutions prevented their further use in this field. Instead, integration-type X-ray area detectors, such as imaging plates (Amemiya *et al.*, 1988, 1995; Amemiya, 1995), fiber-optic tapers/CCDs (Gruner *et al.*, 2002), and image intensifiers/CCDs (Amemiya *et al.*, 1995), have rapidly replaced the MWPCs. They are suitable for use in synchrotron

radiation facilities because they afford position resolution and sensitivity, and can operate under intense radiation. A new type of photon-counting area detector, the micro-strip gas chamber (MSGC), which features fine position resolution ( $\sim 100\ \mu\text{m}$ ), has been studied since the 1990s. Recently, MICROMEAS (Giomataris *et al.*, 1996) and RAPID (Lewis *et al.*, 1997; Berry *et al.*, 2003) have been developed, and have helped meet the challenges of crystallography in high X-ray flux environments.

As an improved and evolutionary version of the MSGC, we have developed a micro-pixel gas chamber ( $\mu$ -PIC), a micro-pattern gaseous detector for radiation imaging (Ochi, Nagayoshi *et al.*, 2001). An anode electrode structure surrounded by cathode rings prevents discharges in the  $\mu$ -PIC (Ochi *et al.*, 2002; Nagayoshi *et al.*, 2003); thus, it is more robust for discharges. An X-ray diffraction study using the continuous rotation photograph (CRP) method in the laboratory was conducted using the  $\mu$ -PIC (Takeda *et al.*, 2005). Photon-counting gaseous detectors such as MSGC have negligible electronics dead-time, whereas integration-type X-ray area detectors have a long electronics dead-time. Moreover, timing measurements of incoming X-ray photons are possible using photon-counting detectors. For this reason, photon-counting gaseous detectors can provide movies of diffraction spots while crystals are rotating. This new scheme, the CRP method, has already been applied with the MSGC (Tanimori *et al.*, 1998; Ochi, Uekusa *et al.*, 2001), and has provided measurements of single-crystal diffraction spots within a few seconds. Takeda *et al.* (2005) demonstrated measurements without electronics dead-time and obtained almost all the diffraction spots while an organic crystal of ylid ( $\text{C}_{11}\text{H}_{102}\text{S}$ ) rotated through  $360^\circ$ . Good internal agreement factors of 3.7% and 7.0% were confirmed among the symmetrically equivalent reflections for exposure times of 3700 and 98 s, respectively.

In this paper we describe the application of the  $\mu$ -PIC to an X-ray area detector optimized for use in synchrotron radiation facilities, and provide details of SAXS experiments performed at SPring-8.

## 2. X-ray area detector using the micro-PIC and GEM

The  $\mu$ -PIC is a micro-pattern gaseous detector fabricated by printed circuit board technology. Fig. 1 shows its schematic structure. X-ray photons are detected by absorption in gas ( $\text{Ar}/\text{C}_2\text{H}_6$  or  $\text{Xe}/\text{C}_2\text{H}_6$ ), followed by induction of electrons, which create pairs. The electrons drift towards a gas electron multiplier (GEM), invented at CERN (Sauli, 1997). The GEM is installed on top of the  $\mu$ -PIC as an intermediate multiplier to increase the gain. We employed a GEM manufactured by Scienergy (Japan). The GEM consists of a polyimide insulator and copper electrodes. The copper electrodes are formed on both sides of the polyimide insulator, with holes of diameter  $50\ \mu\text{m}$ , and placed with a pitch of  $140\ \mu\text{m}$ . The GEM is operated at a gas gain of 10. Electrons are multiplied while passing through the holes in the GEM. The electrons from the GEM drift toward the anodes on the  $\mu$ -PIC and create

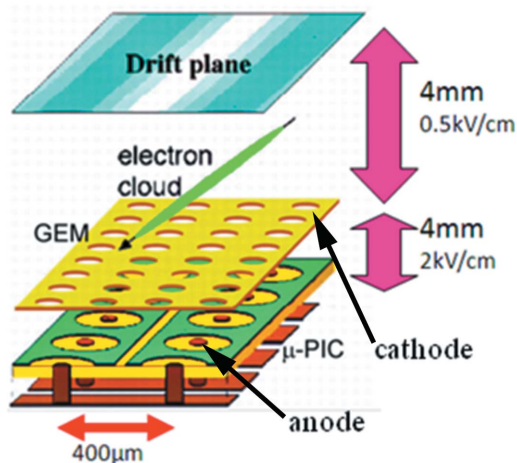


**Figure 1**  
Schematic view of the GEM and  $\mu$ -PIC.

avalanches around the anodes. Figs. 2(a) and 2(b) represent the aspect and an internal view of the  $\mu$ -PIC.

Anode and cathode strips on the  $\mu$ -PIC are formed orthogonally on a polyimide substrate with a pitch of  $400\ \mu\text{m}$ . We employed a strip readout for channel reduction. Anodes are

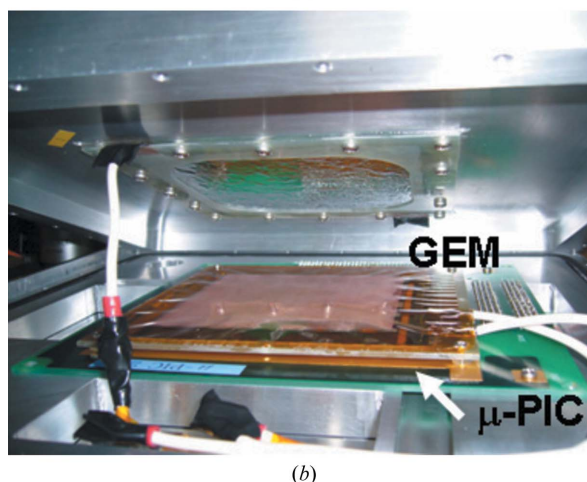
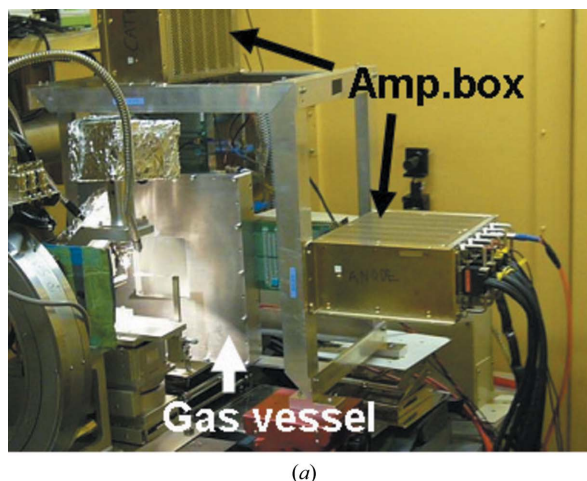


**Figure 2**  
(a) The  $\mu$ -PIC X-ray imaging system at the synchrotron radiation facility, and (b) the GEM on the  $\mu$ -PIC in a vacuum chamber.

located in the center of each pixel and connected by a strip under a 100  $\mu\text{m}$ -thick substrate fabricated by an electric plating process. The electrode geometry was optimized by three-dimensional simulation (Nagayoshi *et al.*, 2004; Bouianov *et al.*, 2005). Here, a  $\mu\text{-PIC}$  with an active area of  $100 \times 100 \text{ mm}$  was employed, manufactured by Dai Nippon Printing. Stable operation was achieved for more than 1000 h at a gas gain of 6000, with an  $\text{Ar}/\text{C}_2\text{H}_6$  (90/10) gas mixture. The gas gain uniformity was 7% (RMS) (Takeda *et al.*, 2004). A two-dimensional position resolution of 120  $\mu\text{m}$  RMS was obtained for continuum X-rays around 10 keV with a  $\text{Xe}/\text{C}_2\text{H}_6$  (70/30) gas mixture.

The GEM was positioned 4 mm from the entrance window. The distance between the GEM and the  $\mu\text{-PIC}$  was also 4 mm. The electric field in the induction region was  $2 \text{ kV cm}^{-1}$  and that in the drift region was  $0.5 \text{ kV cm}^{-1}$ , as shown in Fig. 1. The total gain was over  $10^4$ .

The detector is contained in a sealed vessel with an aluminium entrance window of thickness 0.5 mm. The vessel and the window are designed to withstand a gas pressure of 1 atm to create a vacuum inside the vessel before filling it with gas. The detector is filled with a  $\text{Xe}/\text{C}_2\text{H}_6$  (70/30) gas mixture at a pressure of 1 atm. To connect all electrodes of the  $\mu\text{-PIC}$  to the amplifiers through the gas vessel, we developed a signal extension printed circuit board, which connected the inside of the  $\mu\text{-PIC}$  to IC amplifiers outside the vessel. The extension board was held securely between the upper gas vessel and the bottom plate with O-rings.

The detector's data-acquisition system consists of amplifier-shaper-discriminator (ASD) chips (Orito *et al.*, 2004), a position-encoding module (Kubo *et al.*, 2005) and a memory module on the VME bus. A block diagram of the data-acquisition system is shown in Fig. 3. The output charges of the 256+256 channels are parallel pre-amplified, shaped and discriminated by the ASD chips whose integration time constant is 80 ns. The time constant of signals integrated by the ASD chips was determined by the integration time of charges generated in the  $\mu\text{-PIC}$ . A reference threshold voltage was commonly supplied to all the ASD chips. All discriminated digital signals are sent to the position-encoding module

consisting of FPGAs (field programmable gate arrays) with an internal clock of 100 MHz, allowing recording of the anode and cathode coincident position ( $X, Y$ ) and timing ( $t$ ) in the memory module. Thus, the position encoding is completely executed by digital processing. This method dramatically increased the limits on counting rates to  $>1 \text{ Mcount s}^{-1}$ , while conventional methods based on analogue pulse processing, such as a delay lines and charge division, have achieved a counting rate of several hundred  $\text{kcounts s}^{-1}$ . Moreover, the readouts are simpler and smaller than those of the analogue methods, which adds much to stability and convenience.

In this experiment the ASD reference threshold voltage was set to 25 mV, which corresponds to about  $5 \times 10^4$  electrons, considering both the gain of the ASD chips ( $0.3 \text{ pC V}^{-1}$ ) and the buffer amplification for the ASD comparator (about seven times). This number of electrons corresponds to an energy deposit of about 0.08 keV X-ray photons in Xe gas, when the gas gain is  $10^4$ . An X-ray photon of 13.8 keV generates about 600 primary electrons in Xe gas, which distribute over approximately four strips in the  $\mu\text{-PIC}$ . These electrons are amplified to  $6 \times 10^6$  by the  $\mu\text{-PIC}$  and the GEM. Then, the deposit of the amplified electrons is  $1.5 \times 10^6$  per strip on average, which corresponds to 3 keV. Considering a Gaussian-like distribution of an electron cloud, a 5 keV energy deposit is expected on at least one strip. Despite taking into account the large uncertainty of gains and non-uniformity (a few 10% at maximum), the threshold has sufficient margin for counting loss.

The background counts reached a few counts per second owing to cosmic-ray muons and electrical noise. This counting rate is much lower than the counting rates of X-rays. Thus, the background counts were negligible in the experiments performed at SPring-8.

### 3. Performance characteristics of the micro-PIC for high-count-rate environments

We evaluated the image distortion and linearity in data acquisition rate (DAR) for high-count-rate environments at the RIKEN structural biology beamline I BL45XU at SPring-8, Japan. The wavelength of the X-ray beam,  $\lambda$ , was adjusted to 0.9  $\text{\AA}$ . Its photon flux reached  $10^{12} \text{ photons s}^{-1}$ . A pair of four-blade slits was set in front of a sample to define the beam size, and the beam intensity was adjusted using absorbers installed in front of the first slit. The beam size in front of the sample was a rectangle of size 1.0 mm (horizontal)  $\times$  0.8 mm (vertical). A vacuum path was inserted between the sample and the detector for background reduction, and the  $\mu\text{-PIC}$  was set perpendicular to the X-ray beam. A camera length of 2200 mm was employed. The DAR was examined using a counting rate ranging from

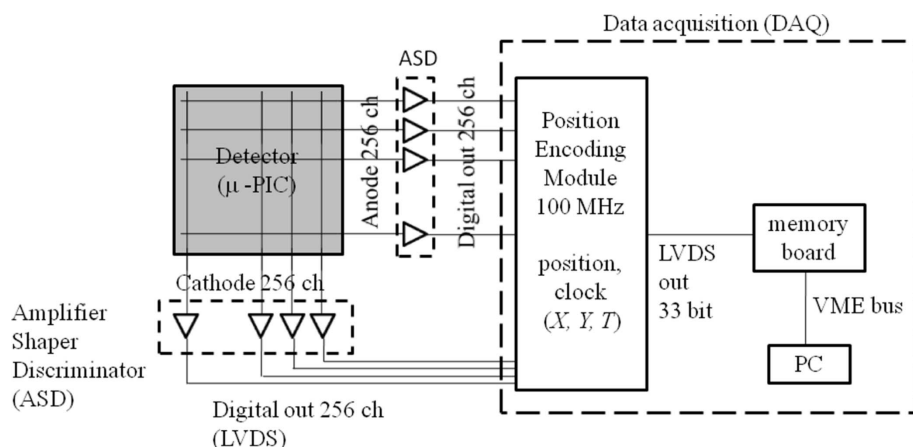


**Figure 3**  
Block diagram of the data-acquisition system.

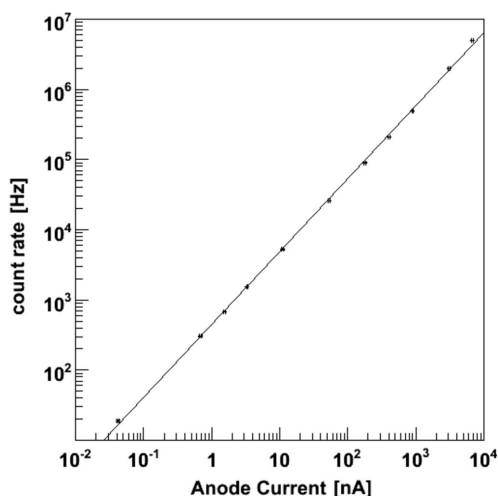


**Figure 4**  
Dynamic range for incident X-ray intensity.

20 counts  $s^{-1}$  to 5 Mcounts  $s^{-1}$ . The leakage current of the  $\mu$ -PIC depended linearly on the beam intensity at the detector. Therefore, we compared the DAR of the  $\mu$ -PIC and its leakage current to evaluate the linearity in the DAR. The image distortion of the  $\mu$ -PIC was investigated by irradiating a grid mask with scattering from a piece of glassy carbon.

The DAR and leakage current demonstrated a good linear correlation from 20 counts  $s^{-1}$  to 5 Mcounts  $s^{-1}$ , as shown in Fig. 4. The current limit of the high-voltage supply module, which supplies current up to 10  $\mu$ A, limits the DAR. The leakage current limit was roughly equivalent to a DAR of 5 Mcounts  $s^{-1}$ .

The DAR of this system is expected to enhance X-rays up to 30 Mcounts  $s^{-1}$ . The encoding system has a transaction rate of up to 100 Mcounts  $s^{-1}$  for synchronous events. However, X-rays usually enter the detector at random, and duplicate hits during a single fetch cycle are rejected by the encoding system. Since the number of events in a single fetch cycle obeys Poisson statistics, the maximum DAR could be close to 30 Mcounts  $s^{-1}$ .

Through measurements, a negligibly small distortion was detected in images of the grid mask. On the grid mask, holes were perpendicularly arranged at the same intervals. The differences in the distance of the holes, as observed by the  $\mu$ -PIC, were within 1% of the entire active area. The deviation from the perpendicular was  $<1^\circ$ . Moreover, the change in the image was negligible when the beam intensity was varied. The peaks observed at the holes on the mask moved 2–8  $\mu$ m when the beam intensity was varied from 8 to 200 kcounts  $s^{-1}$ . We concluded from these results that the strip readout and the coincidence of the strips caused no distortion. Even in the case of micro-pattern gas detectors, an analogue position-encoding method would distort images under moderate count rate environments owing to their readout circuits. In the present evaluation, all image profiles were performed without correction for image distortion.

The detector efficiency is limited by the thickness of the window and gas. The 0.5 mm-thick aluminium window absorbs about 70% of the incident 13.8 keV X-rays, and the 4 mm-

thick Xe gas absorbs only 10% of the X-rays penetrating the window. Thus, only 3% of the X-rays irradiating the detector were detected. We are considering using a carbon-fiber sheet as a window, since it absorbs only 1/32 of the incident 13.8 keV X-rays, allowing detection of 9% of the scattered X-rays. A parallax problem is less critical for SAXS because of the long camera length. For that reason a thicker gas vessel, of 8 mm (twice that of this version), would be possible. The high-transmission window and the thicker gas vessel will provide a detection efficiency of 20%, which leads to an increase in the amount of data and lower statistical uncertainty in the high-angle region. This should widen the dynamic range.

## 4. Verification experiments

### 4.1. Chicken leg collagen

Chicken leg collagen is a standard sample used in the evaluation of imaging detectors in SAXS experiments. The camera length and X-ray wavelength were set to 2200 mm and 0.9  $\text{\AA}$ , respectively. A diffraction pattern from the chicken leg collagen is displayed in Fig. 5(a) using *FIT2D* (Hammersley *et al.*, 1996). There are three dead strips, recognized as blank lines in Fig. 5(a), corresponding to the dead strips on the  $\mu$ -PIC owing to discharges. The total number of events accumulated during 800 s was  $10^8$ . The average counting rate was  $1.2 \times 10^5$  counts  $s^{-1}$ . There is no event-by-event dead-time during data acquisition because each event was continuously accumulated in a memory module. Thus, the data accumulation can be carried out continuously during exposures. Intensity projections to the scattered vector,  $q = 4\pi \sin\theta/\lambda$ , with three different numbers of events,  $10^4$ ,  $10^5$  and  $10^6$ , are plotted in Fig. 5(b), where  $\lambda$  and  $2\theta$  are the X-ray wavelength and scattering angle, respectively. The events are integrated within the fan-shaped area indicated by the solid lines in Fig. 5(a). Note that the clarity of the diffraction patterns was improved drastically by increasing the photon statistics. In addition, the signal-to-noise ratio in the background of the diffraction pattern was also improved. A CCD detector can obtain a similar quality image using multiple exposures, because the exposure time for the CCD detector is limited by saturation for an intense region. In the accumulation of the frames, readout and noise were also accumulated, and, hence, weak peaks were smeared in high-angle regions.

### 4.2. SAXS in solution

Solution X-ray scattering is now widely used for investigation of particle dynamics in a solution. Since the particles take a random orientation in the solution, the directions of scattered X-rays are isotropic and characterized by a function of the scattering angle  $2\theta$ , or of  $q = 4\pi \sin\theta/\lambda$ . The analysis of solution scattering is concerned with the tangent of  $I(q)$  versus  $q$ . Since  $I(q)$  is usually proportional to the power law of  $q$ , a wide dynamic range is crucial for high-precision measurements. To study an effective detector dynamic range, we measured the power-law tendency of the scattering profile of solution scattering from polystyrene (PS) latex, which is

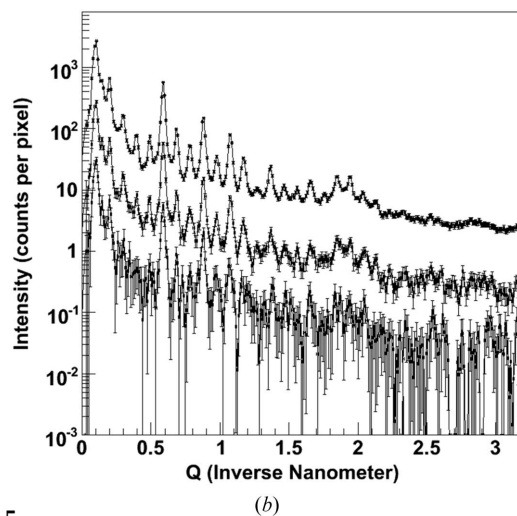
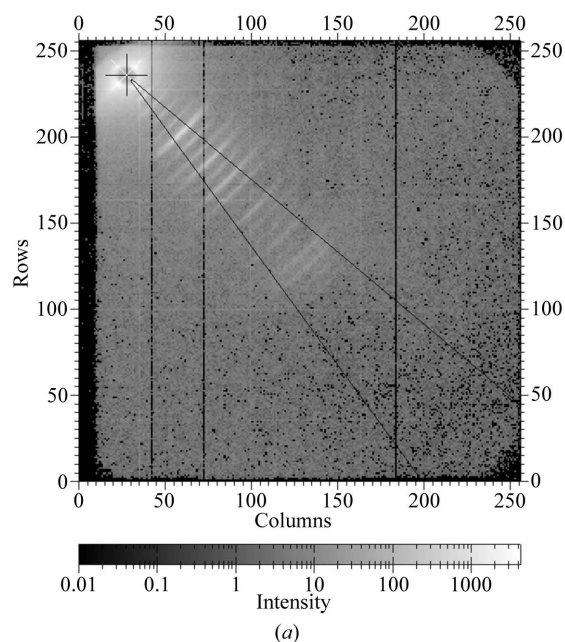


**Figure 5**

(a) Two-dimensional diffraction pattern of collagen; the angular region used to determine the distributions shown in (b) is designated by the diagonal lines. (b) Diffraction patterns of collagen using a  $\mu$ -PIC X-ray imaging system with an accumulation time of  $10^6$  events (top),  $10^5$  events (middle) and  $10^4$  events (bottom).

practically approximated by a solid sphere. Then the scattering intensity of solid spheres, having smooth surfaces, should theoretically follow the  $q^{-4}$  law. We employed solid spheres of diameter 120 nm.

Fig. 6 shows a scattering curve of PS latex accumulated for 200 s with a count rate of 250 kHz at a camera length of 3300 mm. The dynamic range of over  $10^5$  is obtained and the intensity clearly follows a power law of  $q^{-4}$ . In Fig. 6, statistical uncertainty in a high- $2\theta$  region can be observed. This suggests that more data are necessary to confirm that the  $q^{-4}$  power law is followed in the high- $2\theta$  region. The amount of data is limited by the exposure time and detection efficiency.

The exposure time was limited to 200 s to avoid radiation damage of the sample. In fact, this caused the smearing valley of the scattering observed in Fig. 6. Solution scattering has

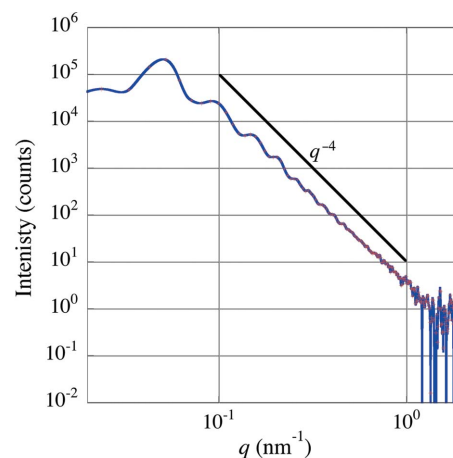


**Figure 6**

Solution scattering patterns from polystyrene latex. The diameter is 120 nm.

already been measured at the same beamline using a MSGC (Toyokawa *et al.*, 2001). At the same time, a dynamic range of  $10^5$  for the MSGC was confirmed, and a time resolution of 500  $\mu$ s was estimated from the SAXS pattern of the pH jump in a protein solution of cytochrome-C from the native state to the denatured state. However, the exposure for solution scattering was 3000 s owing to a limit on beam intensity to prevent the discharge of electrodes in the MSGC. Several measurements were performed while changing samples to avoid radiation damage of the latex. The intense beam was able to irradiate the  $\mu$ -PIC detector, and hence a single measurement provided the same dynamic range. Therefore, based on the results of Toyokawa *et al.* (2001), we were able to deduce that an exposure time of 200 s would correspond to a time resolution of 50  $\mu$ s.

## 5. Conclusion

The performance of a  $\mu$ -PIC system was studied at the RIKEN structural biology beamline (BL45XU-SAXS station) at SPring-8, Japan. The wide dynamic range of the  $\mu$ -PIC system and its tolerance for a high-rate environment were demonstrated. The wide dynamic range realised the detection of higher-order diffraction peaks than the 22nd of collagen in a single measurement. In addition, we analyzed the SAXS pattern of polystyrene latex, and a scattering profile with a dynamic range of  $>10^5$  was achieved. It is expected that the use of a high-transmission window and a thicker gas vessel will realise a dynamic range of  $>10^6$ . The accumulation time was 15 times shorter than that of the MSGC. We also demonstrated a good linear correlation from 20 counts  $s^{-1}$  to 5 Mcounts  $s^{-1}$ . No discharge or gain variation was observed while operating this system over a large number of measurements at SPring-8. Thus, it is concluded that this system has good stability under intense X-rays.

It is expected that counting losses occur when counting rates are over 10 MHz. The strips of the  $\mu$ -PIC should be segmented and sent to several encoding modules to avoid counting losses. Then the total counting rate of the detector

will increase. The PCB technology provides the  $\mu$ -PIC with a very large active area, good gain uniformity and a reasonable cost. We successfully fabricated a  $\mu$ -PIC with a detection area of  $300 \times 300$  mm and demonstrated its stability for a long-duration operation. We employed the same readouts as that of the  $\mu$ -PIC with a detection area of  $100 \times 100$  mm. X-ray imaging using a  $\mu$ -PIC with a large active area is now under investigation. For delivering compact readouts with low power, a CMOS-ASIC chip with amplifiers and discriminators is being developed at KEK, Japan. The number of channels on a chip is doubled to eight channels per chip. These CMOS-ASIC chips will allow all the readout electronics to be located on the rear of the gas vessel, and will make it possible to develop an imaging detector similar to a PC notebook at a quite reasonable cost in a few years.

Many experiments carried out on high-flux and high-brilliance third-generation synchrotron X-ray sources have been limited by the performance of imaging detectors. New photon-counting imaging devices such as the  $\mu$ -PIC will enhance some of these experiments.

We thank the SPring-8 staff for their help and support for this work. We also thank Professor Hideki Seto for his help in using SAXS and an X-ray generator. We are very grateful to Professor Yoshiyuki Amemiya for his noteworthy advice. We extend our appreciation to Rigaku Co. Ltd for their help in using the X-ray generator. This work is supported by KEK Renkei. KT is supported by a Grant-in-Aid from the 21st Century COE 'Centre for Diversity and Universality in Physics', and a Grant-in-Aid in Scientific Research from the Ministry of Education, Culture, Sports, Science and Technology (MEXT). This work was supported by a Grant-in-Aid for the Global COE Program 'The Next Generation of Physics, Spun from Universality and Emergence' from the MEXT of Japan. HU is grateful for the financial support from a Grant-in-Aid for Scientific Research (KAKENHI) in the priority area 'Molecular Nano Dynamics (No. 432)' from MEXT. KH is supported by the Japan Society for the Promotion of Science Research Fellowship for Young Scientists. The synchrotron radiation experiments were performed at BL45XU in SPring-8 with the approval of the Japan Synchrotron Radiation Research Institute (JASRI) (proposals No. 2007A1630, 2007B1407 and 2008A1532).

### References

Amemiya, Y. (1995). *J. Synchrotron Rad.* **2**, 13–21.  
 Amemiya, Y., Ito, K., Yagi, N., Asano, Y., Wakabayashi, K., Ueki, T. & Endo, T. (1995). *Rev. Sci. Instrum.* **66**, 2290–2294.

Amemiya, Y., Matsushita, T., Nakagawa, A., Satow, Y., Miyahara, J. & Chikawa, J. (1988). *Nucl. Instrum. Methods Phys. Res. A*, **266**, 645–653.  
 Berry, A. *et al.* (2003). *Nucl. Instrum. Methods Phys. Res. A*, **513**, 260–263.  
 Bouianov, M., Bouianov, O., Nagayoshi, T., Kubo, H., Miuchi, K., Orito, R., Takada, A., Takeda, A. & Tanimori, T. (2005). *Nucl. Instrum. Methods Phys. Res. A*, **540**, 266–272.  
 Giomataris, Y., Rebourgeard, Ph., Robert, J. P. & Charpak, G. (1996). *Nucl. Instrum. Methods Phys. Res. A*, **376**, 29–35.  
 Gruner, S. M., Tate, M. M. & Eikenberry, E. F. (2002). *Rev. Sci. Instrum.* **73**, 2815–2842.  
 Hammersley, A. P., Svensson, S. O., Hanfland, M., Fitch, A. N. & Häusermann, D. (1996). *High Press. Res.* **14**, 235–248.  
 Kubo, H. *et al.* (2005). *Nucl. Sci. Symp. Conf. Record 2005 IEEE*, **1**, 371–375.  
 Lewis, R. A., Helsby, W. I., Jones, A. O., Hall, C. J., Parker, B., Sheldon, J., Clifford, P., Hillen, M., Sumner, I., Fore, N. S., Jones, R. W. M. & Roberts, K. M. (1997). *Nucl. Instrum. Methods Phys. Res. A*, **39**, 232–241.  
 Nagayoshi, T., Kubo, H., Miuchi, K., Ochi, A., Orito, R., Takada, A., Tanimori, T. & Ueno, M. (2003). *Nucl. Instrum. Methods Phys. Res. A*, **513**, 277–281.  
 Nagayoshi, T., Kubo, H., Miuchi, K., Orito, R., Takada, A., Takeda, A., Tanimori, T., Ueno, M., Bouianov, O. & Bouianov, M. (2004). *Nucl. Instrum. Methods Phys. Res. A*, **525**, 20–27.  
 Ochi, A., Nagayoshi, T., Koishi, S., Tanimori, T., Nagae, T. & Nakamura, M. (2001). *Nucl. Instrum. Methods Phys. Res. A*, **471**, 264–267.  
 Ochi, A., Nagayoshi, T., Koishi, S., Tanimori, T., Nagae, T. & Nakamura, M. (2002). *Nucl. Instrum. Methods Phys. Res. A*, **478**, 196–199.  
 Ochi, A., Uekusa, H., Tanimori, T., Ohashi, Y., Toyokawa, H., Nishi, Y., Nishi, Y., Nagayoshi, T. & Koishi, S. (2001). *Nucl. Instrum. Methods Phys. Res. A*, **467–468**, 1148–1151.  
 Oed, A. (1988). *Nucl. Instrum. Methods Phys. Res. A*, **263**, 351–359.  
 Orito, R., Sasaki, O., Kubo, H., Miuchi, K., Nagayoshi, T., Okada, Y., Takada, A., Takeda, A., Tanimori, T. & Ueno, M. (2004). *IEEE Trans. Nucl. Sci.* **51**, 1337–1342.  
 Phizackerley, R. P., Cork, C. W. & Merritt, E. A. (1986). *Nucl. Instrum. Methods Phys. Res. A*, **246**, 579–595.  
 Sauli, F. (1997). *Nucl. Instrum. Methods Phys. Res. A*, **386**, 531–534.  
 Smith, G. C. (2006). *J. Synchrotron Rad.* **13**, 172–179.  
 Takeda, A., Kubo, H., Miuchi, K., Nagayoshi, T., Okada, Y., Orito, R., Takada, A., Tanimori, T., Ueno, M., Bouianov, O. & Bouianov, M. (2004). *IEEE Trans. Nucl. Sci.* **NS-51**, 2140–2144.  
 Takeda, A., Uekusa, H., Kubo, H., Miuchi, K., Nagayoshi, T., Ohashi, Y., Okada, Y., Orito, R., Takada, A. & Tanimori, T. (2005). *J. Synchrotron Rad.* **12**, 820–825.  
 Tanimori, T., Aoki, S., Nishi, Y. & Ochi, A. (1998). *J. Synchrotron Rad.* **5**, 256–262.  
 Tanimori, T., Ochi, A., Minami, S. & Nagae, T. (1996). *Nucl. Instrum. Methods Phys. Res. A*, **381**, 280–288.  
 Toyokawa, H., Fujisawa, T., Inoko, Y., Nagayoshi, T., Nishi, Y., Nishikawa, Y., Ochi, A., Suzuki, M. & Tanimori, T. (2001). *Nucl. Instrum. Methods Phys. Res. A*, **467–468**, 1144–1147.